A computational study of artery curvature and endograft oversize influence on seal zone behavior in endovascular aortic repair

Žiga Donik [a], Willa Li [b], Blessing Nnate [b], Joseph A. Pugar [b], Nhung Nguyen [b], Ross Milner [b], Enrique Cerda [c], Luka Pocivavsek [b,*], Janez Kramberger [a]

[a] *Faculty of Mechanical Engineering, University of Maribor, Smetanova ulica 17, 2000 Maribor, Slovenia*
[b] *Section of Vascular Surgery and Endovascular Therapy, Department of Surgery, The University of Chicago, 5841 S Maryland Ave, MC 5028, Chicago, IL 60637, USA*
[c] *Departamento de Física, Facultad de Ciencia, Universidad de Santiago de Chile (USACH), Santiago Chile*

ABSTRACT

Thoracic endovascular aortic repair (TEVAR) is a minimally invasive procedure involving the placement of an endograft inside the dissection or an aneurysm to direct blood flow and prevent rupture. A significant challenge in endovascular surgery is the geometrical mismatch between the endograft and the artery, which can lead to endoleak formation, a condition where blood leaks between the endograft and the vessel wall. This study uses computational modeling to investigate the effects of artery curvature and endograft oversizing, the selection of an endograft with a larger diameter than the artery, on endoleak creation. Finite element analysis is employed to simulate the deployment of endografts in arteries with varying curvature and diameter. Numerical simulations are conducted to assess the seal zone and to quantify the potential endoleak volume as a function of curvature and oversizing. A theoretical framework is developed to explain the mechanisms of endoleak formation along with proof-of-concept experiments. Two main mechanisms of endoleak creation are identified: local buckling due to diameter mismatch and global buckling due to centerline curvature mismatch. Local buckling, characterized by excess graft material buckling and wrinkle formation, increases with higher levels of oversizing, leading to a larger potential endoleak volume. Global buckling, where the endograft bends or deforms to conform to the centerline curvature of the artery, is observed to require a certain degree of oversizing to bridge the curvature mismatch. This study highlights the importance of considering both curvature and diameter mismatch in the design and clinical use of endografts. Understanding the mechanisms of endoleak formation can provide valuable insights for optimizing endograft design and surgical planning, leading to improved clinical outcomes in endovascular aortic procedures.

1. Introduction

Aortic disease is a life-threatening condition that poses significant challenges to clinicians in terms of effective diagnosis and treatment. Thoracic aortic aneurysms are pathological dilations of the thoracic aorta that can lead to rupture, with a mortality rate of 94%–100% [1]. Aortic dissections are caused by a separation of the layers of the aortic wall and are classified in the Stanford system as type A if it involves the ascending aorta proximal to the brachiocephalic artery, and type B if it involves the descending aorta distal to the left subclavian artery [2]. Left untreated, acute aortic dissections carry a mortality rate approaching 50% within the first 48 h of onset [2].

A paradigm shift is underway in managing aortic pathology in favor of endovascular repair over open surgery or medical management [3–5]. thoracic endovascular aortic repair (TEVAR) for thoracic

aortic dissections and aneurysms has been shown to decrease pain, hospital length of stay, as well as operative morbidity and mortality, compared to open thoracic aortic surgery [6,7]. Despite these early advantages, endovascular repair is associated with increased intervention rates, higher costs, and inferior long-term survival [4,8–15]. Longitudinal endovascular aortic repair (EVAR)-l trials comparing open and endovascular repair of abdominal aortic aneurysms have shown a crossover in mortality at eight years, favoring open surgery for long-term survival [8].

The EVAR delivery system and covered cylindrical stent design platform were essentially copied for TEVAR, which became clinically dominant in the 2010s, with the total number of thoracic aortic interventions doubling over the last decade [16]. TEVAR failures appear as early as three years, especially in type B aortic dissections (TBAD) [8,

Nomenclature

Abbreviations

ePTFE	Expanded polytetrafluoroethylene
EVAR	Endovascular aortic repair
FDA	The United States Food and Drug Administration
FEA	Finite element analysis
TBAD	Type B aortic dissection
TEVAR	Thoracic endovascular aortic repair

Symbols

α	Scaling factor for the theoretical prediction
β	Bird-beak angle
ϵ	Confinement, oversize
ϵ_0	Critical strain
φ	Vessel angle
κ	Curvature
κ_0	Baseline curvature
λ	Wrinkling wavelength
ν	Poisson's ratio
ρ	Mass density
a	Wrinkling amplitude
$A_{\text{artery lumen}}$	Area of the artery lumen slice
A_{endoleak}	Area of the potential endoleak object slice
C_{10}	Hyperelastic material model parameter
C_{20}	Hyperelastic material model parameter
d	Diameter of the artery
D	Diameter of the endograft
E	Young's modulus
h	Bird-beak height
I_1	First invariant of the left Cauchy–Green deformation tensor
L	Endograft length
N	Number of wrinkles
$PEAR$	Potential endoleak area ratio
$PEVR$	Potential endoleak volume ratio
υ	Experimental endoleak flow rate
$\upsilon_{\text{baseline}}$	Baseline experimental endoleak flow rate
$V_{\text{artery lumen}}$	Volume of the artery lumen
V_{endoleak}	Volume of the potential endoleak object
W	Strain energy density

17–25]. The most common failure modes are attributed to endograft complications, including endoleak, endograft migration, neck dilation, endograft kinking, and material fatigue [26–35]. Endoleaks in particular compromise long-term endograft durability due to continued pressurization of the aneurysmal sac. Type 1 endoleak, caused by an inadequate seal between the aorta and endograft at the proximal and distal attachment sites, can occur in up to 9% of cases and are an indication for reintervention due to a high risk of rupture [36].

In traditional aortic open surgery, the surgical graft is sutured to the aorta, forming a physical structural connection [37]. In endovascular repair, the endograft is placed inside the lumen, where the device and the aorta function as separate entities. The interface between the aortic wall and endograft, called the seal zone, lacks physical coupling and is poorly understood [38,39]. There is a pressing need to comprehensively understand the mechanisms that govern the biomechanical stability of the seal zone as a method to inform greater science-based patient selection with current endograft technologies. A profound understanding of the mechanisms that drive specific interfacial failure modes will allow for the scientifically informed design of the next generations of endografts that can benefit patients for decades post-TEVAR surgery.

The urgency surrounding the long-term failure of endovascular aortic repairs (especially the appearance of endoleaks [27–35,40]) is highlighted by The United States Food and Drug Administration (FDA) in the recent public review showcasing how little the technology has evolved over 30 years [41].

There is a growing clinical appreciation that the uniformly cylindrical endografts designed for the straight thoracic and the thoracoabdominal aorta are not ideally suited for the curvature and the hemodynamic conditions in the distal aortic arch [26]. Proper alignment and conformity of endovascular devices within the aortic seal zone are crucial to prevent complications like endoleak and unfavorable aortic remodeling, which contribute to poor long-term outcomes [26,30,42]. Pocivavsek and Milner [43] were the first to propose a paradigm shift in the mechanical conceptualization of the seal zone as an adhesive interface. They showed that the seal zone can be effectively modeled using the cohesive zone method in the case of a perfectly cylindrical seal [43]. Fundamental to the understanding of the seal zone as a cohesive interface is the formation of an interface between the inside of the aorta and the outside wall of the endograft. First and foremost, forming a reliable interface between the endograft and the aorta depends on the geometric compatibility of these components at the interface. Quantitative studies on the impact of geometric incompatibility on interfacial stability have been attempted for simple shape mismatch systems, such as the adhesion of a flat disk/plate to a curved sphere (contact lens problem) [44]. Such quantitative understanding of the effects of the geometric incompatibility induced by deploying a cylindrical endograft in complex aortic geometry on seal zone stability is lacking.

Despite TEVAR being widely accepted in clinical practice, a more rigorous scientific understanding of the mechanisms underpinning failure modes, such as endoleak, is required. This knowledge would help identify the surgical procedure best suited to a specific patient's anatomy and support the creation of technological and design frameworks to inform the next generation of devices [26–35,37–41,45–54].

The use of numerical simulations is gaining importance and building trust in biomechanics, with researchers pushing the boundaries of mechanistic understanding of biological principles. The integration of simulations has become standard in the design process of endovascular devices, significantly shortening development timelines and enhancing outcomes. FEA has been used to simulate the deployment of devices inside idealized and patient-specific anatomies. In the last decade, several authors have reported computational simulations of stent-grafts, investigating different aspects of aortic stenting. Their studies utilize numerical simulations and computational frameworks to analyze endovascular repair and stent-graft deployment in the ascending aorta, comparing postoperative images with corresponding simulations of custom-treated pseudoaneurysms [19,55], analyzing post-TEVAR bird-beak configurations [56], and addressing the impact of Nitinol stent design on contact and radial force effectiveness [57]. Several numerical simulation studies based on the finite element method have been published dealing with the use of stent-grafts in the aorta. It has been shown that information from personalized computational simulations can significantly assist the clinician in pre-surgical planning [58]. Another relevant study aims to provide a realistic and robust computational framework to support TEVAR planning in clinical practice, including post-TEVAR hemodynamic studies [59]. The recent literature review strongly emphasizes the importance of the credibility and reliability of a computational model for reproducing the clinical TEVAR procedure [60,61].

FEA has been shown to be an efficient tool to model endograft deployment but has yet to be applied to provide mechanistic insights
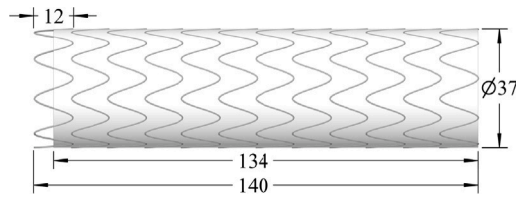
Fig. 1. Structure and dimensions of the stent-graft, which is comprised of a polymer graft and 12 metal stent support rings. At the proximal end, there is an uncovered bare metal region extending by half the amplitude of the ring modeling a free flow configuration. The total length of the graft is 140 mm and its diameter is fixed at 37 mm. The peak–trough length of a stent support ring is 12 mm.

Vessel angle, φ	0°, 30°, 60°				
Oversizing	0%	5%	10%	20%	25%
Diameter, d / mm	37.00	35.24	33.64	30.83	29.60

Fig. 2. Dimensions of the artery. The diameter d of the vessel is parametrized to achieve different oversizing ratios. Different vessel curvatures are achieved by changing the angle φ between the proximal and the distal end of the artery. On both ends of the artery, there is a 30 mm long straight portion, and the rest of the artery is curved with a centerline arc length of 140 mm. The wall thickness is uniform and equal to 3 mm.

into how the endograft oversizing and axial positioning (correlated to aortic curvature) dictate interfacial stability.

This paper presents a distinct view of the endograft-aorta seal zone with a volumetric analysis of the potential endoleak. Numerical simulations are used to deploy highly realistic TEVAR devices of different oversizes inside model arteries with varying curvatures. Motivating our study is the clinical knowledge that oversizing is the only operational control parameter in endograft selection while aortic curvature is the anatomic variant that must be considered. The current work provides a critical step towards the full development of the elasto-adhesive seal zone model [43]. We show that a complete interface between the endograft and aorta exists only in a limited region of the curvature-oversizing parameter space. The appearance and characterization of non-contacting regions within the seal zone is the primary focus of this paper. Our hypothesis is that such regions serve as the first mode of failure within the seal zone, since they are effectively failed contact zones within which blood can accumulate or flow. The volume contained within the non-contacting regions is our primary output and presented as the potential endoleak volume ratio (*PEVR*). *PEVR* is shown to develop by two mechanisms: a local buckling of the endograft membrane driven by oversizing and a global buckling of the cylindrical endograft when constrained in a curved aorta. Strategies that minimize *PEVR* through better patient selection or improved endograft designs are likely to minimize future endoleaks.
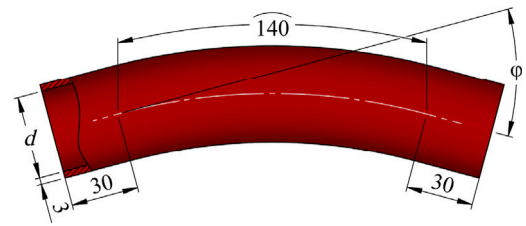
2. Methods

The study employed FEA to investigate the mechanics of a covered TEVAR endograft inside an artery with varying curvature and stent-graft oversizing. Fifteen configurations are constructed by combining three different curvatures (0°, 30°, and 60°) and five different oversizing ratios (0%, 5%, 10%, 20%, and 25%). Stent-graft deployment inside the vessel is simulated in LS-DYNA [62], and the resulting deformed geometry is then post-processed and examined using Blender [63]. A simple experimental setup is also designed to compare against the simulation data, and a theoretical model is derived to predict the potential endoleak in straight cylindrical confined geometries.

Finite element analysis

A model of a generic stent-graft with a length of 140 mm and diameter of 37 mm is created in Gmsh [64]. Sinusoidal curves with nine peaks are used to create the 12 support rings of the stent. The dimensions of the stent-graft are shown in Fig. 1. The diameter of the wire is 0.5 mm and the thickness of the graft fabric is 0.2 mm.

The curved artery is parametrically modeled in different configurations, depending on the curvature and oversizing ratio. The dimensions of the artery along with the parameters are shown in Fig. 2. Given the greater complexity of creating the stent versus the artery, we decided to use a single stent model and change the artery geometry to study various degrees of oversizing and curvature. Clinically, this is equivalent to using the same device in various patient anatomies.

Dynamic explicit analysis is performed in LS-DYNA to simulate the stent-graft deployment inside each of the artery models. The endograft is meshed in Gmsh with a combination of beam (metal support rings) and membrane (graft fabric) finite elements with shared nodes, allowing the stent-graft to deform as a single part without additional constraints. Linear Hughes–Liu beam elements with cross-section integration (ELFORM = 1) and triangular fully integrated Belytchko–Tsay membrane elements (ELFORM = 9) are used. Based on the performed convergence study (see Appendix A for details), the selected beam and membrane element size is 0.7 mm and 1 mm, respectively. The artery is meshed with 8-noded hexahedral solid elements (ELFORM = 2) with three elements through the thickness and global element size of 2.3 mm. Both ends of the artery are fully constrained.

A hyperelastic material model proposed by Vorp and Raghavan [65] is used for the artery. The strain energy function is defined as $W = C_{10}(I_1-3)+C_{20}(I_1-3)^2$, where I_1 is the first invariant of the left Cauchy–Green deformation tensor, and C_{10} and C_{20} are material constants, for which the values are acquired in the literature [66] ($C_{10} = 0.174$ MPa and $C_{20} = 1.881$ MPa). The Poisson's ratio, v, is set to 0.49 and the mass density, ρ, to 1000 kg/m^3 [67]. The Nitinol (Ni-Ti alloy) rings of the stent-graft are modeled as linear elastic with Young's modulus of 83 GPa, Poisson's ratio of 0.33 and density of 6450 kg/m^3 [68]. A neo-Hookean material model is used for the graft fabric (ePTFE) with the initial shear modulus of 1353 MPa and density of 3360 kg/m^3 [69].

The endograft is compressed to the lumen diameter, bent to align to the artery centerline, and finally released to expand and conform to the arterial wall. This deformation of the stent-graft is guided by a crimper tool, modeled as a shell tube with a diameter of 37 mm and thickness of 1 mm made of steel (linear elastic: $E = 210$ GPa, $v = 0.3$, $\rho = 7850$ kg/m^3). Each node of the crimper has a prescribed displacement curve to perform the desired motion. The described steps of the analysis are shown in Fig. 3. Pressure of 10 kPa (75 mmHg) is applied to the internal surface of the endograft to simulate mean aortic pressures experienced by the luminal surface of the graft post-deployment.

The symmetric general contact formulation (*CONTACT_AUTOMATIC_GENERAL) with a friction coefficient of 0.1 is utilized in LS-DYNA. This contact algorithm is adept at handling all element types (beam, shell, membrane, and solid) and is applied to all contacts. During simulation steps involving compression, bending, and expansion of the endograft, the crimper–endograft contact is employed. Prior to the stent-graft expansion phase, the endograft–artery contact definition is initiated, and once the expansion phase is complete, the crimper–endograft contact is deactivated.
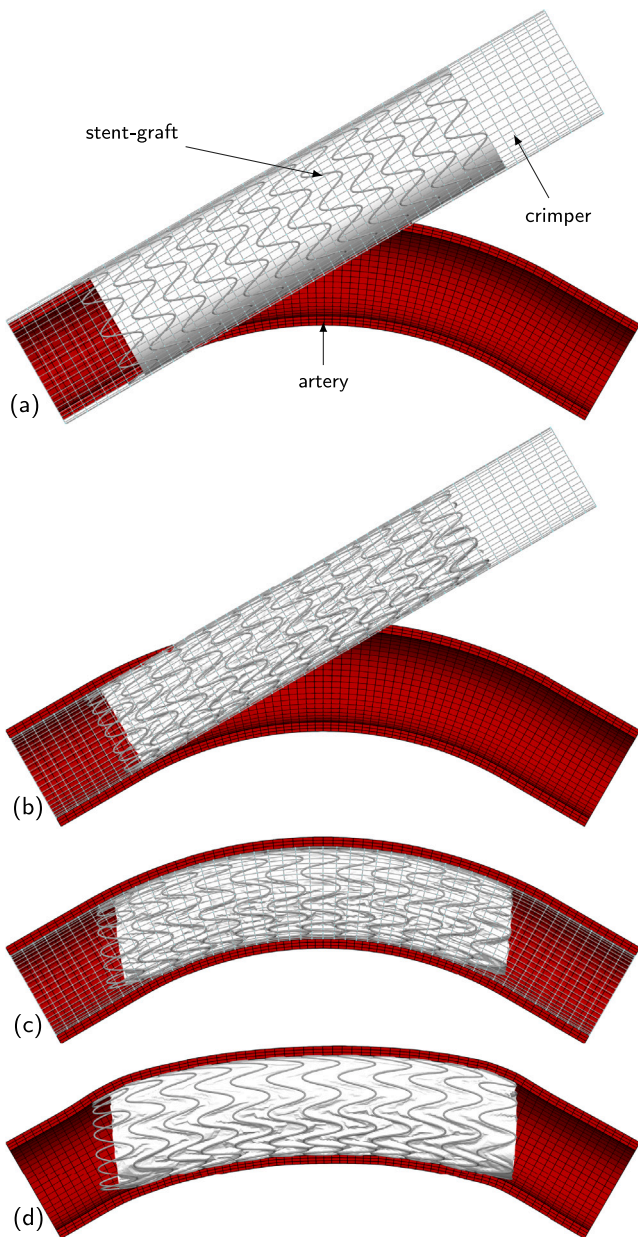
Fig. 3. Stent-graft deployment procedure in FEA: (a) initial configuration, (b) crimping, (c) bending (forming), and (d) deployment (expansion). A prescribed displacement is applied to each node of the crimping tool (gray wireframe) to satisfy the required movement to deploy the endograft (white) inside the artery (red). The finite element mesh of the artery and the crimper is also visible. The artery is shown in section view for better visibility.

Volumetric analysis

The resulting deformed geometry (shell graft and solid artery) of each model is exported from LS-DYNA as an STL file and imported into Blender for further processing and analysis. Each beam element is represented by two nodes, and therefore cannot be exported in STL format, which contains triangular surfaces made of three points. A Python script in Blender is used to create a 3D geometry from beam elements. The imported graft surface is thickened inside Blender to create a 3D solid body of the graft. A volumetric analysis is performed in Blender using Boolean operations. A new object is created to represent the lumen of the artery. The stent-graft is then used to cut the artery lumen and create a new object representing the potential endoleak volume. The

objects used for the volumetric analysis are shown in Fig. 4. The volume of the potential endoleak and the volume of the artery lumen are then measured and used to calculate the potential endoleak volume ratio (*PEVR*) for each model: $PEVR = \frac{V_{\text{endoleak}}}{V_{\text{artery lumen}}}$.

The endoleak object is manually checked for volumetric integrity to identify gaps and separate volumes. Partitioned volumes are then colored differently for visualization.

An additional analysis is then done to see how the endoleak volume is distributed in the axial direction. A Python script is used to create multiple slicing planes along the artery centerline (acquired with VMTK [70]) according to stent support rings placement. A total of 24 slicing planes are created and placed at the center and the end of each support ring, as shown in Fig. 5. Those slicing planes are then used to cut the potential endoleak object and the artery lumen object to get the cross-sectional area of the potential endoleak and the artery lumen at each slicing plane. The ratio is then calculated to get the normalized potential endoleak area ratio (*PEAR*) at each slicing plane: $PEAR = \frac{A_{\text{endoleak}}}{A_{\text{artery}}}$. The *PEAR* is then plotted against the normalized axial position on the artery centerline.

Experimental setup

A proof-of-concept experiment is also designed to compare against simulation data. We hypothesize that these computational predictions for the potential of endoleak can be tested by measuring and comparing the leak rates through seal zones of varying degrees of geometric mismatch. Cylindrical endografts are deployed inside clear Tygon tubes (McMaster-Carr) with different diameters to obtain various oversizing ratios. A 25 mm graft inside a 25 mm tube, a 30 mm graft inside a 25 mm tube, and a 25 mm graft inside a 20 mm tube correspond to 0, 20, and 25% oversize, respectively. The angulation of each endograft–tube pair is increased from 0° to 30°, and 60°, as shown in Fig. 6. A total of nine endograft–tube configurations are tested. An additional test on a tube without an endograft is used to establish a baseline.

The tubes are connected to a pulsatile water pump (Harvard Apparatus) which controls the fluid flow through the tube lumen. Tap water is used with the flow rate of 400 mL/min. To measure leakage, a well-controlled 4 mm hole is induced in the lesser curve of the bent wall of the Tygon tube in the seal zone. The higher potential for endoleak is hypothesized to be associated with a faster rate of fluid leaking through a hole in the tube wall in the seal zone. Therefore, we measure the volume of the fluid leaking through the puncture in a fixed timeframe to acquire the leak rate (Fig. 7).

The experiments are limited by only having access to fixed sizes of tubing and stents which restrict the geometries and available oversizing ratios. The use of manual manipulation of the tubes to impose varying degrees of angulation might also limit the consistency of the experimental results.

Theoretical prediction

A simple mathematical model is derived in 2D to predict the wrinkling of a thin tubular membrane under cylindrical confinement for 0° angulation. The confinement of the endograft with diameter *D* inside the aorta with diameter *d*, where $D \geq d$ is assumed. The endograft has to be radially compressed to fit inside the artery, therefore forming wrinkles on the surface to bridge the geometric incompatibility (Fig. 8). The wrinkling occurs in the circumferential direction. The potential place for the endoleak is the volume between the endograft and the artery wall, which can be approximated. Membrane inextensibility provides the classic relationship between wrinkle amplitude *a*, the wrinkling wavelength λ, and confinement ϵ [71,72]:

$$a \sim \frac{\lambda}{\pi}\sqrt{\epsilon - \epsilon_0} \tag{1}$$

The confinement (i.e., oversize) ϵ can be expressed as a function of the diameters of the endograft and the artery: $\epsilon = (D - d)/d$. The initial
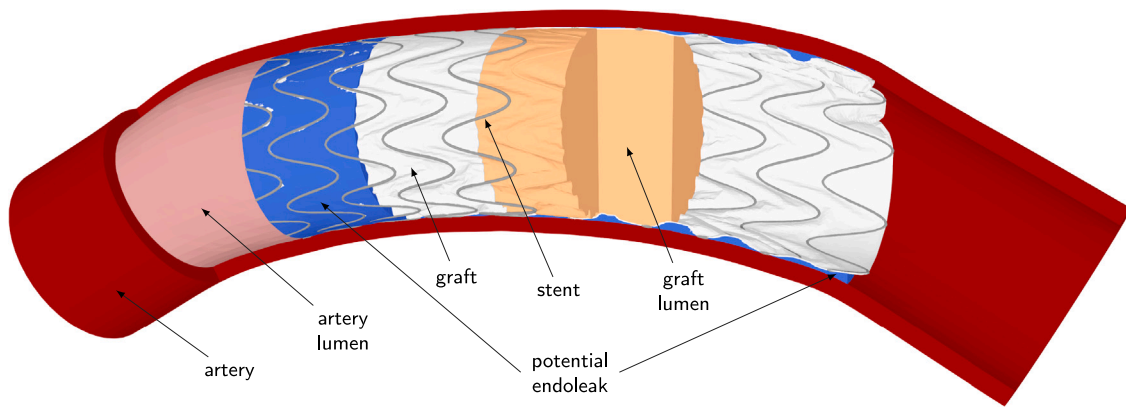
Fig. 4. Objects used for the volumetric analysis and for calculating the potential endoleak ratio in Blender. Artery and the stent-graft were imported from the FEA as deformed geometry. The remaining objects were created in Blender with Boolean operations. *PEVR* is the ratio of the potential endoleak volume (blue) and the artery lumen volume (pink).
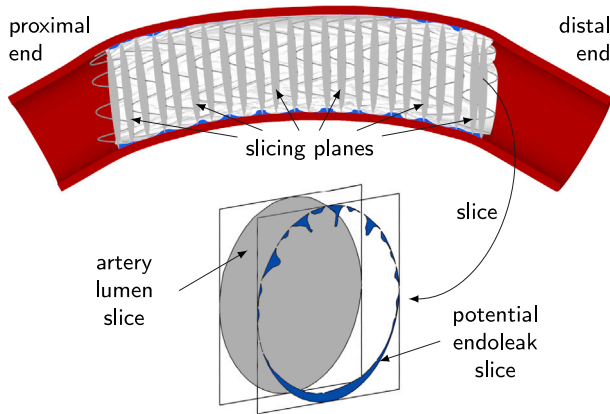

Fig. 5. Slicing planes defined to extract the artery lumen area and the potential endoleak area at different positions along the vessel centerline. The artery is shown in its lengthwise cross-sectional view. The planes are aligned to the stent support rings (peaks and middle portions). Each plane creates a slice of endoleak and the artery lumen, which are then used to calculate the area ratio at each location along the endograft. *PEAR* is the ratio of the blue area to the gray area at each slice.
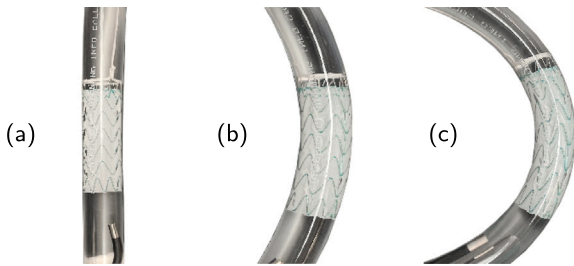

Fig. 6. The angulations of the tube for the experiment: (a) 0°, (b) 30°, and (c) 60°.
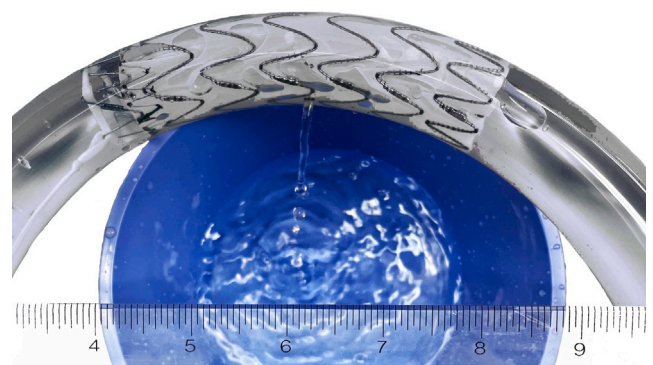

Fig. 7. The leak rate measurement setup for the experiment. A hole is created in the lesser curve of the tube in the seal zone area, and the volume of the fluid that leaked out is measured in a fixed timeframe to calculate the leak rate. A baseline is established by measuring the leak rate of the punctured tube without the endograft.
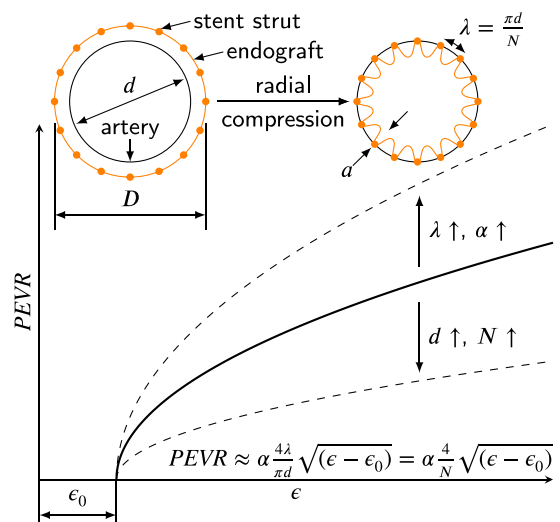

Fig. 8. The theoretical system is composed of an artery with a fixed diameter d and the endograft with a diameter D, that is compressed to fit inside the artery, geometrically confining the endograft and forming wrinkles on the surface. The wrinkling wavelength λ corresponds to the spacing between the stent struts.

confinement ϵ_0 is the oversize of the endograft before the wrinkling occurs.

The potential endoleak volume depends on the amplitude a, the wrinkling wavelength λ, the length of the endograft L, and the number of wrinkles N ($N = \pi d / \lambda$). The number of wrinkles also corresponds to the number of stent struts on the section of the endograft. Substituting N and a into the equation, the potential endoleak volume transforms to:

$$V_{\text{endoleak}} = a\left(\lambda N\right) L = \lambda \sqrt{\epsilon - \epsilon_0}\, d\, L \tag{2}$$

The *PEVR* is defined as a ratio between the endoleak volume (Eq. (2)), and the volume of the artery lumen ($V_{\text{artery lumen}} = \pi d^2 L / 4$).

We added a scaling factor α and the initial confinement ϵ_0 (shifting the curve on the x-axis) to help fit the theoretical prediction to the experimental data. Substituting and simplifying, we get the equation
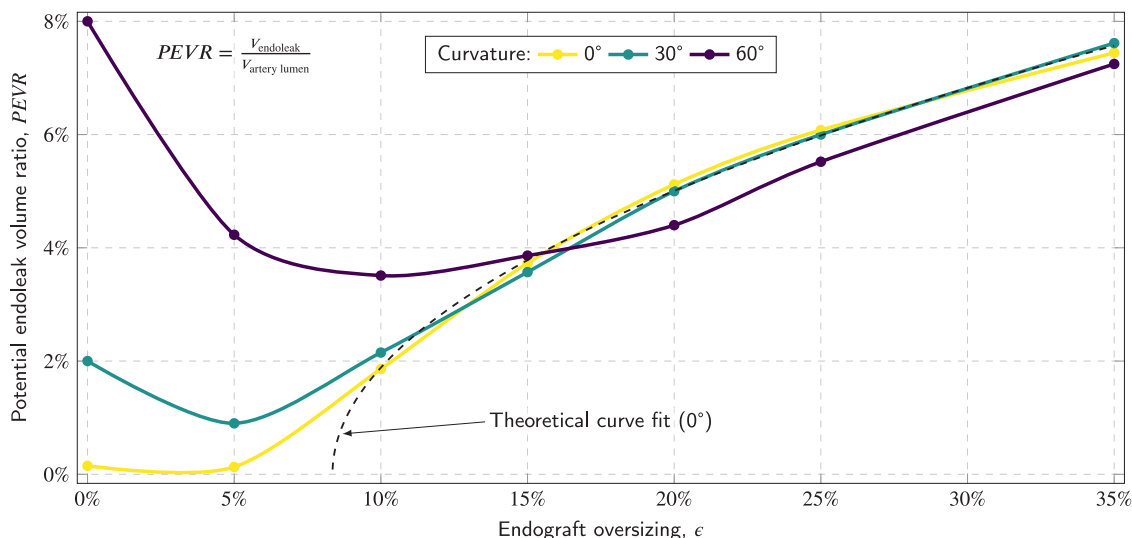
Fig. 9. The potential endoleak volume ratio (*PEVR*) for different stent-graft oversizing and artery curvatures. The potential endoleak generally increases with oversizing. That could be attributed to the wrinkling of the graft material when compressed and the amplitude of the wrinkles increasing with more compression (larger oversizing). The larger amplitude of the wrinkles can be linked to a larger potential endoleak volume. The increase of the *PEVR* with larger oversizing is almost linear with the 0° while the 30° and 60° curvatures show an increase in the potential endoleak at 0% oversizing (also 5% oversizing at 60°). Higher vessel curvatures require larger endograft oversizing to overcome the geometric incompatibility between the straight endograft and the curved artery. The theoretical curve fit (Eq. (3), $N = 9$) corresponding to the 0° configuration is also shown with a dashed line. The fitting parameters $\alpha = 0.33$ and $\epsilon_0 = 8.35\%$ were determined by fitting the theoretical curve to the 0° data points and calculating the minimum sum of squared residuals.

to theoretically predict the *PEVR*.

$$PEVR \approx \alpha \frac{4\lambda}{\pi d} \sqrt{(\epsilon - \epsilon_0)} = \alpha \frac{4}{N} \sqrt{(\epsilon - \epsilon_0)} \qquad (3)$$

3. Results and discussion

The results from the volumetric analysis show how artery curvature and endograft oversizing influence the potential for endoleak. The *PEVR* for different curvature-oversize configurations is presented in Fig. 9. Each curve on the graph represents one of the artery angulations, that is 0°, 30°, or 60°.

Our results show that endoleak volumes relate to oversizing and curvature in a highly non-linear bimodal mechanism (Fig. 9). The first source of non-linearity is from graft buckling or wrinkling. In the zero-curvature case (yellow curve in Fig. 9), a classic buckling instability is observed, where stent oversizing is directly proportional to circumferential compressive strain, $\epsilon = (D - d)/d$. Of note, ϵ can be re-written in terms of curvatures, $\epsilon = (\kappa_0 - \kappa)/\kappa$; from this vantage, oversizing can also be viewed as a curvature-mismatch problem, where the relevant curvatures are set by the inverse radii of the aorta and stent-graft. Buckling instabilities are known to have a critical strain, ϵ_0, beyond which a sinusoidal deformation of the initially flat surface grows. This is observed in our simulations, where *PEVR* remains zero until $\epsilon = 5\%$. Beyond this critical strain, *PEVR* grows with a square root dependence on strain. The excellent agreement between the wrinkle-based theoretical calculation and the simulation results (dashed black line and yellow line in Fig. 9) allows us to conclude that the endograft fabric buckles with a wavelength λ set by stent ring spacing ($\pi d/N$) and an amplitude that behaves like traditional wrinkles.

The wrinkling pattern is clearly evident when looking at the axial cross-sections as shown in Fig. 10. Interestingly, the square-root dependence holds even though the wrinkling amplitude is not monotonic along the axial length of the stent-graft. The theoretical analysis is two-dimensional and the theoretical endoleak volume in Eq. (2) is obtained by simply multiplying with L. However, as Fig. 11 shows, the cross-sectional area, *PEAR*, fluctuates along the longitudinal (L) axis. These fluctuations can be understood from the standpoint that the membrane is tethered to the metal stent ring, and as such, when the membrane approaches the metal its amplitude is dampened. Despite this
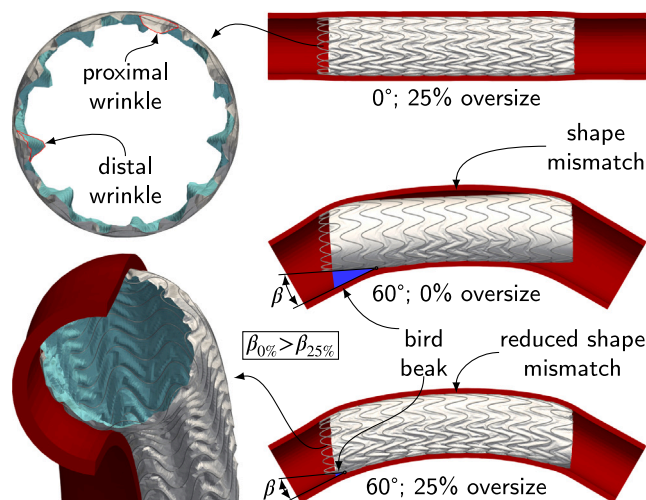

Fig. 10. Endograft behavior with increasing geometric incompatibility. The inner surface of the endograft is colored differently for better visibility. The wrinkling on the oversized configurations is caused by the diameter mismatch and occurs in the radial direction. The wrinkling amplitude on the distal end is almost twice as high as on the proximal end of the graft. This is due to the stent-graft structure, where the fabric fully covers the stent struts on the distal end, and only half of the support ring is covered on the proximal end, ensuring a shorter wrinkling wavelength and, consequently, lower amplitude. With increasing vessel curvature, the geometric incompatibility manifests in bird-beak formation and separation of the arterial wall and the endograft at the middle of the interface. The effect is more noticeable with 0% oversizing, where there are some minor wrinkles on the lesser curve, but the rest of the graft is stretched out, especially on the greater curve side. More excess material in the form of wrinkles helps reduce the geometric incompatibility, allowing the greater curve side to stretch in the longitudinal direction, also reducing the bird-beak angle (β).

modulation, the two-dimensional wrinkle model captures the overall endoleak volume well in the zero-curvature case. Lastly, the observed membrane buckling is stable despite the addition of 10 kPa of luminal graft pressure. This last observation is key, since clinically, vascular surgeons often operate under the assumption that small amplitude graft 'infolding' or wrinkling, is collapsed by blood pressure; indeed,
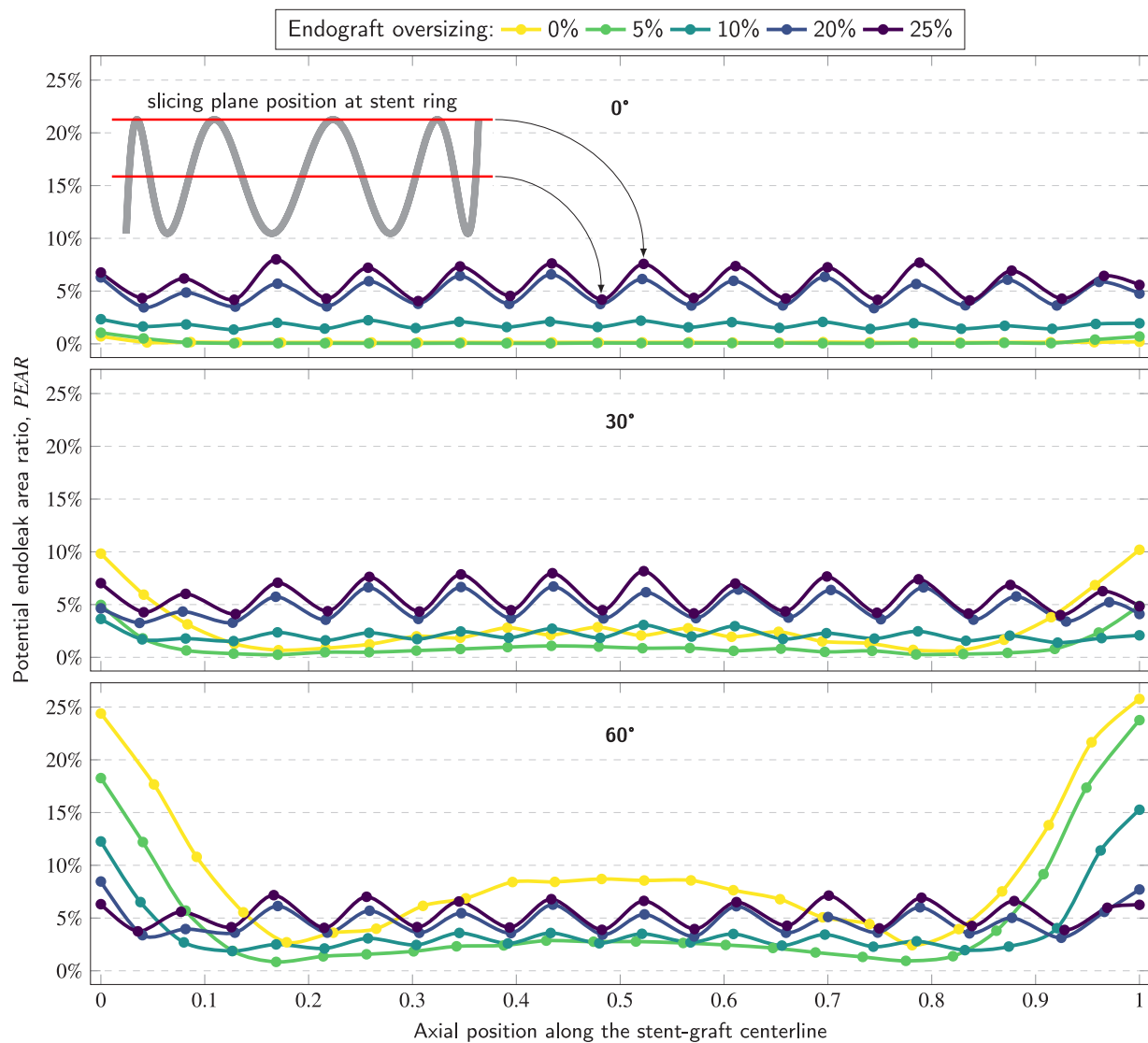
Fig. 11. Potential endoleak area ratio (*PEAR*) along the stent-graft for different oversizing ratios and curvatures (0°, 30°, and 60°). The figure shows the distribution of the potential endoleak along the stent-graft. At 0°, the potential endoleak is evenly distributed along the whole endograft. The volume created between the artery and the stent-graft is the result of the wrinkling of the stent-graft, the amplitude of which increases with oversizing. The sine wave-like pattern, that is more pronounced at higher oversizing ratios, can be attributed to the locations of the slicing planes. The wrinkling amplitude and wavelength changes according to the position on the stent-graft. When the slice is positioned along the middle of the stent support ring, the wavelength is about half of the wavelength to when the slice is in line with the peaks of the stent support ring. The larger wavelength is linked to larger amplitude of the wrinkle and therefore larger potential endoleak.

our simulations disprove this empirical hypothesis. In conclusion, the first source of non-linearity in endoleak volumes arise from the local buckling–wrinkling instability of the compressed graft membrane and can be best observed in the zero axial curvature simulations.

The second source of non-linearity in endoleak volume scaling enters with the mismatch in the reference centerline curvature of the artery and graft. The zero-stress configuration of the endograft is the straight cylindrical tube. The aorta however has axial curvature. Geometrically such surfaces are mismatched in their metric since the Gaussian curvature of the graft reference configuration is zero while that of the aorta is non-zero and spatially varying. In this paper, we reduce the metric mismatch to a mismatch in centerline angulation which is 0° for the graft reference configuration and 0°, 30°, or 60° for the model aortas. The isolated impact of axial curvature mismatch is seen in the 0% oversizing data for the three aortic angles in Figs. 9 and 11.

Qualitatively, the data can be understood by considering the flexural rigidity of the stent along the centerline. The confined stent is initially forced to bend onto the geometry of the arterial center line (this mimics the centerline wire in a TEVAR procedure). However, once deployed, the final configuration is one that minimizes the elastic energy of the stent, which includes its flexural bending energy along the center line. The graft will naturally tend towards a straight cylinder unless boundary forces arising from contact with the arterial wall change the balance of forces. In the case of 0% oversizing, there is very little to no contact with the aortic wall, as such the initially curved graft always returns to its straight cylindrical reference configuration (see Fig. 10). This generates a large amount of volume between the two surfaces which is represented in the rapidly rising *PEVR* with increased angles. Fig. 11 shows that the distribution of this volume is also non-linear along the length of the graft.

The largest contribution to the endoleak volume coming from the proximal and distal ends of the stent (near 0 and 1 on the abscissa in Fig. 11). This is clinically significant since such configurations when observed during TEVAR are termed bird-beaking, a known risk factor for endoleak formation [73–75]. Unlike for the circumferential wrinkles, there is no simple mechanical model that accounts for the marked increase in endoleak volume with increasing curvature.
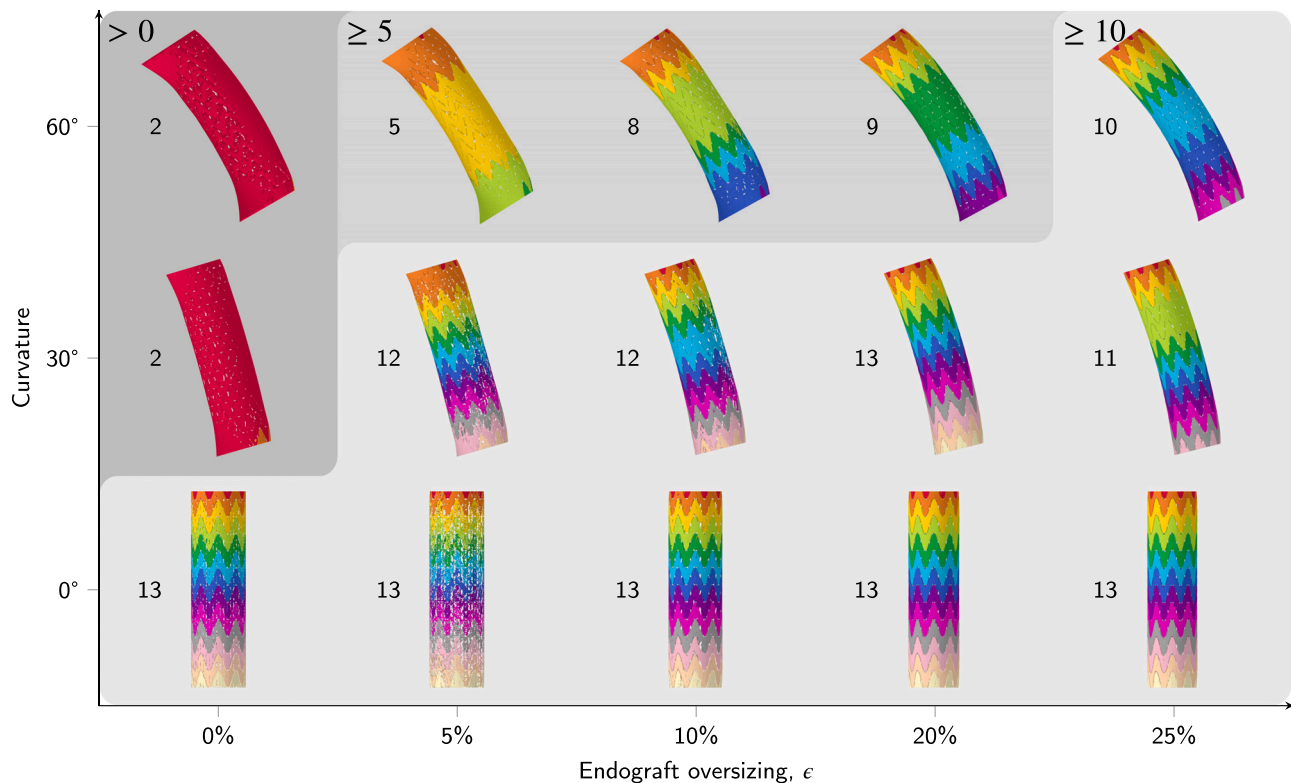
Fig. 12. Number of disconnected potential endoleak zones for each of the 15 configurations depending on vessel curvature and stent-graft oversizing. Different colors represent separate potential endoleak pockets. The number of disconnected zones is shown next to each model. The models are divided into three groups based on the number of separate zones (>0, ≥5, and ≥10). The models in the first group (>0) only have two separate endoleak volumes, which means that there is no contiguous seal zone created by the stent-graft that would span the entire circumference of the stent support ring. The higher the number of disconnected potential endoleak zones, the higher the number of established seals at endograft support rings and the lower the risk of endoleak. As the vessel curvature increases, the stent-graft oversizing should also be increased to ensure better geometric conformity and a broader seal zone.

A simple geometric analysis does give some insight into the observed linear decrease in bird-beak volume with oversizing. We observe that the free ends of the stent are rotated such that they are not normal to the artery centerline (see Fig. 10, 60°, 0% oversizing). By construction, the bird-beak angle β is equal to the proximal rotation of the endograft relative to the normal to the aortic centerline. Bird-beak height is given by $h = d \left(\frac{1}{\cos \beta} - 1 \right)$. So for bird-beak angle $\beta = 30°$, bird-beak height becomes $h = 0.15d$, which is in agreement with Fig. 10. Oversizing does not change this free end stent rotation (compare 0% and 25% oversizing in Fig. 10). Oversizing closes the bird-beak volume by extending the stent in its rotated plane. This analysis predicts that for a stent diameter of $D = \frac{d}{\cos \beta} = \frac{2\sqrt{3}}{3}d = 1.15d$ per 25% oversizing and 60° vessel curvature ($\beta = 30°$), the bird-beak volume is obliterated. Indeed this is observed in Fig. 12 for 60° at axial position 0 (proximal end) and 1 (distal end).

The point where a given *PEVR* curve approaches the wrinkle scaling law defines the critical oversizing beyond which axial curvature no longer plays a significant role in setting endoleak volume (10% for 30°, and 15% for 60°). From the standpoint of TEVAR, these are significant observations. First, the known high-risk bird-beak volumes can be reduced with a standard endograft but only at the expense of oversizing. Second, the reduction in this volume is highly non-linear. Third, the degree of curvature mismatch dictates how much oversizing is necessary to push the endograft into a conformed configuration. Fourth, even in the conformed configuration there is still substantial endoleak volume, however the source is now from local graft wrinkling. We conclude that for moderate angulation (30°) 5% oversizing would be ideal, while for greater angulation (60°) 10%–15% oversizing minimizes the endoleak volume.

Lastly, we examined the topology of the endoleak volume regions as a function of their distance along the endograft (Fig. 12). The lack of graft membrane apposition to the aortic wall is the dominant source of endoleak volume, however the metal stent portion of the graft may also lose contact depending on the arterial geometry. Such lack of stent ring apposition has been studied previously [76,77]. We show that stent ring apposition is always a function of metric mismatch, i.e., it occurs only with axial curvature of the aorta. There is a strong correlation between loss of stent ring apposition and endoleak volume that arises from centerline curvature mismatch. We observe that the oversizing cross-over point where the graft again regains greater than 10 separate zones (Fig. 12) is similar to the critical oversizing at which the *PEVR* data approaches the theoretical wrinkle scaling.

The experimental results shown in Fig. 13 are in good agreement with the trend obtained from numerical simulations (Fig. 9). At 0% oversize and 0° angulation, the perfectly matched shape of the cylindrical endograft and the tube has the lowest potential for endoleak. At this oversize, the potential endoleak rate grows with increasing vessel curvature due to a more significant endograft–tube geometric mismatch. As the oversize increases, the effect of the geometric incompatibility between the stent-graft and the curved tube becomes less dominant. That can be observed from the smaller spread of the data points at the 20%–25% oversize range compared to the 0%–20% oversize range.

For the three experimentally tested oversize values (0%, 20%, and 25%), leaking is increased with oversizing. The experimental results are consistent with the simulation data, where the potential endoleak volume is measured. Interestingly, at smaller oversize, we see a non-monotonic trend in the potential endoleak in simulations, suggesting a threshold for oversize where the two mechanisms of wrinkling form a
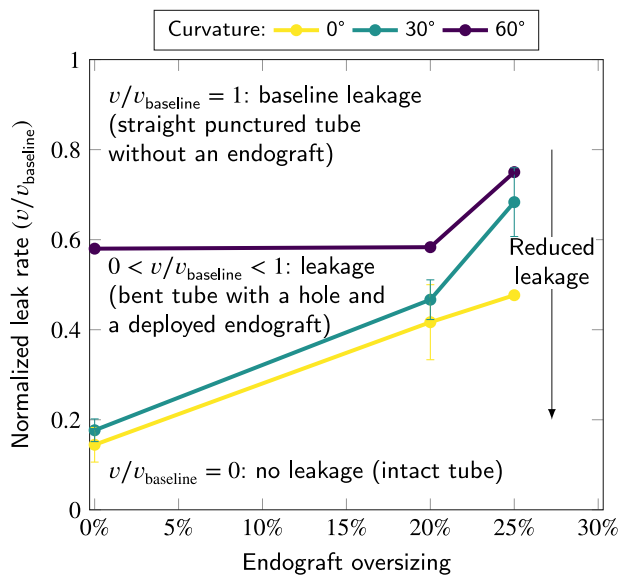
Fig. 13. Experimental data for the normalized leak rate v/v_{baseline} obtained from the flow rate measurements for three different endograft oversizing values (0%, 20%, and 25%) and three different tube bending angles (0°, 30°, and 60°). The results show a similar trend to the numerical simulations, where the potential endoleak volume ratio is measured. The leak rate grows with increasing oversize, and the 60° configuration shows an increased potential endoleak volume even at lower oversize ratios, which is consistent with the non-monotonic trend predicted in the numerical simulations.

minimum endoleak value. A signature of this non-monotonicity is also seen in experimental data for the 60° bent shape, where no significant leak rate difference is seen between 0% and 20% oversize, as opposed to 0° and 30° angulations.

4. Conclusions

Type 1 endoleak is the Achilles heel of endovascular aortic surgery [15,17]. There is growing clinical consensus that lack of stable proximal seal is the reason only one-third of endovascular aneurysm repairs show meaningful signs of aneurysm shrinkage and healing [18,25,30, 37,42,48–54,78]. As noted in the introduction, our prior work has conceptualized the mechanical stability of the seal zone within the framework of an adhesive interface.

In this paper, we quantitate the volume and area, *PEVR* and *PEAR*, respectively, between the above two surfaces that form the seal zone interface. We hypothesize that this volume and area are surrogate measures of the potential endoleak, since blood can only flow through some existing gap within the seal zone. Using *PEVR* and *PEAR* allows us to analyze our high-fidelity finite element simulations of stent-graft deployment in various geometries and draw quantitative conclusions about potential endoleaks as a function of oversizing and aortic curvature.

Taking a cylindrical neck with zero-degree curvature oversized by 10%–15% as a clinical gold standard allows us to state that under physiologic conditions a *PEVR* under 2%–4% does not generate a clinically significant endoleak. Using this cut-off, we see that a standard TEVAR with minimal to no oversizing will be at substantial risk for endoleak formation purely based on geometric considerations. In this regime, the dominant source of endoleak volume is from the metric mismatch of the two surfaces and not from local graft wrinkling. This observation should influence future graft designs which should be optimized to minimize the metric mismatch between the aortic surface and endograft and thereby reduce the potential endoleak volume.

Table 1
Detailed results of the mesh convergence study conducted on seven models with varying element sizes, including the selected mesh number 6 with beam element size of 0.7 mm and membrane element size of 1.0 mm.

i	Maximum beam element size/mm	Maximum membrane element size/mm	$PEVR$	Computation time
1	2.34	3.35	0.84%	≈11 h
2	1.76	2.51	4.70%	≈14 h
3	1.41	2.00	12.8%	≈17 h
4	1.17	1.68	7.67%	≈21 h
5	0.88	1.26	7.64%	≈28 h
6	0.70	1.00	7.85%	≈35 h
7	0.57	0.81	7.80%	≈48 h

CRediT authorship contribution statement

Žiga Donik: Writing – original draft, Visualization, Software, Methodology, Conceptualization. **Willa Li:** Investigation. **Blessing Nnate:** Investigation. **Joseph A. Pugar:** Methodology. **Nhung Nguyen:** Writing – review & editing, Validation, Methodology. **Ross Milner:** Funding acquisition, Conceptualization. **Enrique Cerda:** Writing – review & editing, Methodology. **Luka Pocivavsek:** Writing – review & editing, Writing – original draft, Supervision, Project administration, Funding acquisition, Conceptualization. **Janez Kramberger:** Writing – review & editing, Supervision, Project administration, Funding acquisition.

Declaration of competing interest

The authors declare that they have no known competing financial interests or personal relationships that could have appeared to influence the work reported in this paper.

Appendix A

A.1. Mesh convergence study

A mesh convergence study is conducted for the straight artery configuration with the largest oversizing (35%). The primary result of the FEA is the *PEVR*, which is used as the parameter to compare different mesh sizes. The maximum beam and membrane element sizes for each of the tested finite element meshes are also provided. The mesh sensitivity analysis results are presented in Table 1. The *PEVR* obtained with the chosen mesh, which has a maximum beam element size of 0.7 mm and a maximum membrane element size of 1.0 mm, is within less than 1% of the *PEVR* obtained with the finest tested mesh.

Appendix B. Supplementary data

Supplementary material related to this article can be found online at https://doi.org/10.1016/j.compbiomed.2024.108745.

References

[1] R. Gouveia e Melo, G. Silva Duarte, A. Lopes, M. Alves, D. Caldeira, R. Fernandes e Fernandes, L. Mendes Pedro, Incidence and prevalence of thoracic aortic aneurysms: A systematic review and meta-analysis of population-based studies, Semin. Thorac. Cardiovasc. Surg. 34 (2022) 1–16, http://dx.doi.org/10.1053/j.semtcvs.2021.02.029.

[2] D. Levy, A. Goyal, Y. Grigorova, F. Farci, J.K. Le, Aortic dissection, in: StatPearls [Internet], StatPearls Publishing, Treasure Island (FL), 2023.

[3] M. Czerny, M. Grimm, D. Zimpfer, S. Rodler, R. Gottardi, D. Hutschala, J. Lammer, E. Wolner, M. Schoder, Results after endovascular stent graft placement in atherosclerotic aneurysms involving the descending aorta, Ann. Thorac. Surg. 83 (2007) 450–455, http://dx.doi.org/10.1016/j.athoracsur.2006.08.031.

[4] S. De Bock, F. Iannaccone, M. De Beule, F. Vermassen, P. Segers, B. Verhegghe, What if you stretch the IFU? A mechanical insight into stent graft instructions for use in angulated proximal aneurysm necks, Med. Eng. Phys. 36 (2014) 1567–1576, http://dx.doi.org/10.1016/j.medengphy.2014.08.003.

[5] M.M. Frohlich, G.-Y. Suh, J. Bondesson, M. Leineweber, J.T. Lee, M.D. Dake, C.P. Cheng, Thoracic aortic geometry correlates with endograft bird-beaking severity, J. Vasc. Surg. 72 (2020) 1196–1205, http://dx.doi.org/10.1016/j.jvs.2019.11.045.

[6] E.C. Kuo, N. Veranyan, C.E. Johnson, F.A. Weaver, S.W. Ham, V.L. Rowe, F. Fleischman, M. Bowdish, S.M. Han, Impact of proximal seal zone length and intramural hematoma on clinical outcomes and aortic remodeling after thoracic endovascular aortic repair for aortic dissections, J. Vasc. Surg. 69 (2019) 987–995, http://dx.doi.org/10.1016/j.jvs.2018.06.219, URL: https://pubmed.ncbi.nlm.nih.gov/30528404/.

[7] D. Li, L. Peng, Y. Wang, J. Zhao, D. Yuan, T. Zheng, Predictor of false lumen thrombosis after thoracic endovascular aortic repair for type B dissection, J. Thorac. Cardiovasc. Surg. 160 (2020) 360–367, http://dx.doi.org/10.1016/j.jtcvs.2019.07.091, URL: https://pubmed.ncbi.nlm.nih.gov/31558276/.

[8] R. Patel, M.J. Sweeting, J.T. Powell, R.M. Greenhalgh, EVAR trial investigators, Endovascular versus open repair of abdominal aortic aneurysm in 15-years' follow-up of the UK endovascular aneurysm repair trial 1 (EVAR trial 1): a randomised controlled trial, Lancet 388 (2016) 2366–2374, http://dx.doi.org/10.1016/S0140-6736(16)31135-7.

[9] S. De Bock, F. Iannaccone, G. De Santis, M. De Beule, D. Van Loo, D. Devos, F. Vermassen, P. Segers, B. Verhegghe, Virtual evaluation of stent graft deployment: A validated modeling and simulation study, J. Mech. Behav. Biomed. Mater. 13 (2012) 129–139, http://dx.doi.org/10.1016/j.jmbbm.2012.04.021.

[10] E.D. Dillavou, S.C. Muluk, R.Y. Rhee, E. Tzeng, J.D. Woody, N. Gupta, M.S. Makaroun, Does hostile neck anatomy preclude successful endovascular aortic aneurysm repair? J. Vasc. Surg. 38 (2003) 657–663, http://dx.doi.org/10.1016/S0741-5214(03)00738-9.

[11] D. Perrin, N. Demanget, P. Badel, S. Avril, L. Orgéas, C. Geindreau, J.-N. Albertini, Deployment of stent grafts in curved aneurysmal arteries: Toward a predictive numerical tool, Int. J. Numer. Methods Biomed. Eng. 31 (2015) 1–11, http://dx.doi.org/10.1002/cnm.2698.

[12] G.A. Pitoulias, A.R. Valdivia, S. Hahtapornsawan, G. Torsello, A.G. Pitoulias, M. Austermann, C. Gandarias, K.P. Donas, Conical neck is strongly associated with proximal failure in standard endovascular aneurysm repair, J. Vasc. Surg. 66 (6) (2017) 1686–1695, http://dx.doi.org/10.1016/j.jvs.2017.03.440, URL: https://www.sciencedirect.com/science/article/pii/S0741521417311126.

[13] A. Schanzer, R.K. Greenberg, N. Hevelone, W.P. Robinson, M.H. Eslami, R.J. Goldberg, L. Messina, Predictors of abdominal aortic aneurysm sac enlargement after endovascular repair, Circulation 123 (2011) 2848–2855, http://dx.doi.org/10.1161/circulationaha.110.014902.

[14] Y. Seike, T. Fukuda, K. Yokawa, Y. Inoue, T. Shijo, K. Uehara, H. Sasaki, H. Matsuda, Preoperative neck angulation is associated with aneurysm sac growth due to persistent type ia endoleak after endovascular abdominal aortic aneurysm repair, Ann. Vasc. Dis. 13 (2020) 261–268, http://dx.doi.org/10.3400/avd.oa.20-00057.

[15] United Kingdom EVAR Trial Investigators, R.M. Greenhalgh, L.C. Brown, J.T. Powell, S.G. Thompson, D. Epstein, M.J. Sculpher, Endovascular versus open repair of abdominal aortic aneurysm, N. Engl. J. Med. 362 (2010) 1863–1871, http://dx.doi.org/10.1056/NEJMoa0909305.

[16] I.S. Hasan, J.A. Brown, D. Serna-Gallegos, E. Aranda-Michel, S. Yousef, Y. Wang, I. Sultan, Association of thoracic aortic aneurysm versus aortic dissection on outcomes after thoracic endovascular aortic repair, J. Am. Heart Assoc. 12 (2023) e027641, http://dx.doi.org/10.1161/JAHA.122.027641.

[17] M. Boufi, F. Aouini, C. Guivier-Curien, B. Dona, A.D. Loundou, V. Deplano, Y.S. Alimi, Examination of factors in type I endoleak development after thoracic endovascular repair, J. Vasc. Surg. 61 (2015) 317–323, http://dx.doi.org/10.1016/j.jvs.2014.08.002.

[18] M.M. Marrocco-Trischitta, B. Spampinato, G. Mazzeo, D. Mazzaccaro, V. Milani, M. Alaidroos, F. Ambrogi, G. Nano, Impact of the bird-beak configuration on postoperative outcome after thoracic endovascular aortic repair: A meta-analysis, J. Endovasc. Therapy 26 (2019) 771–778, http://dx.doi.org/10.1177/1526602819865906.

[19] F. Auricchio, M. Conti, S. Marconi, A. Reali, J.L. Tolenaar, S. Trimarchi, Patient-specific aortic endografting simulation: From diagnosis to prediction, Comput. Biol. Med. 43 (2013) 386–394, http://dx.doi.org/10.1016/j.compbiomed.2013.01.006.

[20] R.J. Hinchliffe, A. Krasznai, L. SchultzeKool, J.D. Blankensteijn, M. Falkenberg, L. Lönn, K. Hausegger, M. de Blas, J.M. Egana, B. Sonesson, K. Ivancev, Observations on the failure of stent-grafts in the aortic arch, Eur. J. Vasc. Endovasc. Surg. 34 (2007) 451–456, http://dx.doi.org/10.1016/j.ejvs.2007.06.005.

[21] Z.H. Dong, W.G. Fu, Y.Q. Wang, D.Q. Guo, X. Xu, Y. Ji, B. Chen, J.H. Jiang, J. Yang, Z.Y. Shi, T. Zhu, Y. Shi, Retrograde type a aortic dissection after endovascular stent graft placement for treatment of type b dissection, Circulation 119 (2009) 735–741, http://dx.doi.org/10.1161/circulationaha.107.759076.

[22] J. Kpodonu, O. Preventza, V.G. Ramaiah, H. Shennib, G.H. Wheatley III, J. Rodriquez-Lopez, J. Williams, E.B. Diethrich, Retrograde type a dissection after endovascular stenting of the descending thoracic aorta. Is the risk real? Eur. J. Cardio Thorac. Surg. 33 (2008) 1014–1018, http://dx.doi.org/10.1016/j.ejcts.2008.03.024.

[23] M. Malina, J. Brunkwall, K. Ivancev, B. Lindblad, J. Malina, U. Nyman, B. Risberg, Late aortic arch perforation by graft-anchoring stent: Complication of endovascular thoracic aneurysm exclusion, J. Endovasc. Surg. 5 (1998) 274–277, http://dx.doi.org/10.1177/152660289800500317, URL: https://www.ncbi.nlm.nih.gov/pubmed/9761584.

[24] T. Kölbel, T. Lee, K. Ivancev, T.A. Resch, B. Sonesson, M. Malina, In situ bending of a thoracic stent-graft: A proposed novel technique to improve thoracic endograft seal, J. Endovasc. Therapy 15 (2008) 62–66, http://dx.doi.org/10.1583/07-2257.1.

[25] C.-A. Behrendt, A. Sedrakyan, H.C. Rieß, F. Heidemann, T. Kölbel, J. Petersen, E.S. Debus, Short-term and long-term results of endovascular and open repair of abdominal aortic aneurysms in Germany, J. Vasc. Surg. 66 (2017) 1704–1711.e3, http://dx.doi.org/10.1016/j.jvs.2017.04.040.

[26] B.W. Ullery, K. Tran, 18 - Complications in endovascular thoracoabdominal aortic aneurysm repair, in: M.L. Dryjski, L.M. Harris (Eds.), Complications in Endovascular Surgery, Elsevier, Philadelphia, 2022, pp. 117–126, http://dx.doi.org/10.1016/B978-0-323-55448-0.00018-8.

[27] F.B. Goncalves, S.E. Hoeks, J.A. Teijink, F.L. Moll, J.A. Castro, R.J. Stolker, T.L. Forbes, H.J.M. Verhagen, Risk factors for proximal neck complications after endovascular aneurysm repair using the Endurant stentgraft, Eur. J. Vasc. Endovasc. Surg. 49 (2015) 156–162, http://dx.doi.org/10.1016/j.ejvs.2014.10.003.

[28] G.A. Antoniou, G.S. Georgiadis, S.A. Antoniou, G. Kuhan, D. Murray, A meta-analysis of outcomes of endovascular abdominal aortic aneurysm repair in patients with hostile and friendly neck anatomy, J. Vasc. Surg. 57 (2013) 527–538, http://dx.doi.org/10.1016/j.jvs.2012.09.050.

[29] A. Hemmler, B. Lutz, C. Reeps, G. Kalender, M.W. Gee, A methodology for in silico endovascular repair of abdominal aortic aneurysms, Biomech. Model. Mechanobiol. 17 (2018) 1139–1164, http://dx.doi.org/10.1007/S10237-018-1020-0.

[30] W.D. Jordan, K. Ouriel, M. Mehta, D. Varnagy, W.M. Moore, F.R. Arko, J. Joye, J.-P.P. de Vries, W.D. Jordan, J.P. de Vries, J. Joye, H. Eckstein, J. van Herwaarden, F.R. Arko, P. Bove, W. Bohannon, B. Fioole, C. Setacci, T. Resch, V. Riambau, D. Scheinert, A. Schmidt, D. Clair, M. Moursi, M. Farber, J. Tessarek, G. Torsello, M. Fillinger, M. Glickman, J. Henretta, K. Hodgson, J. Jim, B. Katzen, E. Lipsitz, M. Cox, T. Naslund, V. Ramaiah, M. Schermerhorn, P. Schneider, B.W. Starnes, C. Donayre, M. Mehta, B. Zipfel, N. Malhotra, D. Varnagy, W. Moore, N. Cheshire, C. Bicknell, M. Back, B. Muhs, M.B. Malas, S. Hussain, N. Gupta, D. Bockler, E. Verhoeven, M. Reijnen, Outcome-based anatomic criteria for defining the hostile aortic neck, J. Vasc. Surg. 61 (6) (2015) 1383–1390.e1, http://dx.doi.org/10.1016/j.jvs.2014.12.063, URL: https://www.sciencedirect.com/science/article/pii/S0741521415000658.

[31] E.M. Marone, A. Freyrie, C. Ruotolo, S. Michelagnoli, M. Antonello, F. Speziale, P. Veroux, M. Gargiulo, A. Gaggiano, Expert opinion on hostile neck definition in endovascular treatment of abdominal aortic aneurysms (a delphi consensus), Ann. Vasc. Surg. 62 (2020) 173–182, http://dx.doi.org/10.1016/j.avsg.2019.05.049.

[32] M.M. Marrocco-Trischitta, H.W. de Beaufort, F. Secchi, T.M. van Bakel, M. Ranucci, J.A. van Herwaarden, F.L. Moll, S. Trimarchi, A geometric reappraisal of proximal landing zones for thoracic endovascular aortic repair according to aortic arch types, J. Vasc. Surg. 65 (2017) 1584–1590, http://dx.doi.org/10.1016/j.jvs.2016.10.113.

[33] C.O. McDonnell, M. Halak, A. Bartlett, S.R. Baker, Abdominal aortic aneurysm neck morphology: Proposed classification system, Irish J. Med. Sci. 175 (2006) 4–8, http://dx.doi.org/10.1007/BF03169164.

[34] R.C. Schuurmann, K. Ouriel, B.E. Muhs, W.D. Jordan, R.L. Ouriel, J.T. Boersen, J.P.P. de Vries, Aortic curvature as a predictor of intraoperative type ia endoleak, J. Vasc. Surg. 63 (2016) 596–602, http://dx.doi.org/10.1016/j.jvs.2015.08.110, URL: https://pubmed.ncbi.nlm.nih.gov/26796290/.

[35] R.C. Schuurmann, K. van Noort, S.P. Overeem, R. van Veen, K. Ouriel, W.D. Jordan Jr., B.E. Muhs, Y.W. 't Mannetje, M.M. Reijnen, B. Fioole, Ç. Ünlü, P. Brummel, J.-P.P. de Vries, Determination of endograft apposition, position, and expansion in the aortic neck predicts type ia endoleak and migration after endovascular aneurysm repair, J. Endovasc. Therapy 25 (2018) 366–375, http://dx.doi.org/10.1177/1526602818764616.

[36] S. Ameli-Renani, V. Pavlidis, R.A. Morgan, Secondary endoleak management following TEVAR and EVAR, Cardiovasc Intervent Radiol 43 (2020) 1839–1854, http://dx.doi.org/10.1007/s00270-020-02572-9.

[37] R. Milner, Rethinking EVAR: Is longer seal zone the only answer for enhancing durability? Endovasc. Today 17 (2018) 24–27.

[38] E.J. Turney, S.P. Steenberge, S.P. Lyden, M.J. Eagleton, S.D. Srivastava, T.P. Sarac, R.L. Kelso, D.G. Clair, Late graft explants in endovascular aneurysm repair, J. Vasc. Surg. 59 (2014) 886–893, http://dx.doi.org/10.1016/j.jvs.2013.10.079.

[39] T. McGloughlin, Biomechanics and Mechanobiology of Aneurysms, vol. 7, Springer Berlin, Heidelberg, Berlin, Heidelberg, 2011, http://dx.doi.org/10.1007/978-3-642-18095-8.

[40] R.C. Schuurmann, K. van Noort, S.P. Overeem, K. Ouriel, W.D. Jordan Jr., B.E. Muhs, Y. 'T Mannetje, M. Reijnen, B. Fioole, Ç. Ünlü, P. Brummel, J.-P.P. de Vries, Aortic curvature is a predictor of late type ia endoleak and migration after endovascular aneurysm repair, J. Endovasc. Therapy 24 (2017) 411–417, http://dx.doi.org/10.1177/1526602817700378.

[41] The United States Food and Drug Administration (FDA), FDA advisory panel recommendations on lifelong surveillance and long-term postmarket data collection for patients with AAA endovascular aortic repair — Letter to health care providers, 2022, https://www.fda.gov/medical-devices/letters-health-care-providers/fda-advisory-panel-recommendations-lifelong-surveillance-and-long-term-postmarket-data-collection. (Accessed 30 September 2022).

[42] P. Cao, F. Verzini, G. Parlani, P. De Rango, B. Parente, G. Giordano, S. Mosca, A. Maselli, Predictive factors and clinical consequences of proximal aortic neck dilatation in 230 patients undergoing abdominal aorta aneurysm repair with self-expandable stent-grafts, J. Vasc. Surg. 37 (2003) 1200–1205, http://dx.doi.org/10.1016/s0741-5214(02)75340-8.

[43] L. Pocivavsek, R. Milner, Dynamic seal at the aortic neck-endograft interface studied using a novel method of cohesive zone modeling, J. Vasc. Surg. 72 (2019) 703–713.e3, http://dx.doi.org/10.1016/j.jvs.2019.07.101.

[44] J. Hure, B. Roman, J. Bico, Wrapping an adhesive sphere with an elastic sheet, Phys. Rev. Lett. 106 (2011) 174301, http://dx.doi.org/10.1103/PhysRevLett.106.174301.

[45] C.A. Figueroa, C.K. Zarins, Computational analysis of displacement forces acting on endografts used to treat aortic aneurysms, in: T. McGloughlin (Ed.), Biomechanics and Mechanobiology of Aneurysms, Springer Berlin, Heidelberg, Berlin, Heidelberg, 2011, pp. 221–246, http://dx.doi.org/10.1007/8415_2011_73.

[46] M.L. Dijkstra, C.J. Zeebregts, H.J.M. Verhagen, J.A.W. Teijink, A.H. Power, D. Bockler, P. Peeters, V. Riambau, J.-P. Becquemin, M.M.P.J. Reijnen, Incidence, natural course, and outcome of type II endoleaks in infrarenal endovascular aneurysm repair based on the ENGAGE registry data, J. Vasc. Surg. 71 (2020) 780–789, http://dx.doi.org/10.1016/j.jvs.2019.04.486.

[47] K.H.J. Ultee, S. Büttner, R. Huurman, F.B. Gonçalves, S.E. Hoeks, W.M. Bramer, M.L. Schermerhorn, H.J.M. Verhagen, Editor's choice - systematic review and meta-analysis of the outcome of treatment for type II endoleak following endovascular aneurysm repair, Eur. J. Vasc. Endovasc. Surg. 56 (2018) 794–807, http://dx.doi.org/10.1016/j.ejvs.2018.06.009.

[48] B.E. Muhs, W. Jordan, K. Ouriel, S. Rajaee, J.-P. de Vries, Matched cohort comparison of endovascular abdominal aortic aneurysm repair with and without EndoAnchors, J. Vasc. Surg. 67 (2018) 1699–1707, http://dx.doi.org/10.1016/j.jvs.2017.10.059.

[49] S.R. Goudeketting, K. van Noort, J.J.M. Vermeulen, K. Ouriel, W.D. Jordan Jr., J.M. Panneton, C.H. Slump, J.-P.P.M. de Vries, Analysis of the position of EndoAnchor implants in therapeutic use during endovascular aneurysm repair, J. Vasc. Surg. 69 (2019) 1726–1735, http://dx.doi.org/10.1016/j.jvs.2018.09.035.

[50] W.D. Jordan Jr., M. Mehta, K. Ouriel, F.R. Arko, D. Varnagy, J. Joye, W.M. Moore, J.-P.P.M. de Vries, One-year results of the ANCHOR trial of EndoAnchors for the prevention and treatment of aortic neck complications after endovascular aneurysm repair, Vascular 24 (2016) 177–186, http://dx.doi.org/10.1177/1708538115590727.

[51] A.R. Valdivia, A. Chaudhuri, R. Milner, G. Pratesi, M.M.P.J. Reijnen, G. Tinelli, R. Schuurmann, M. Barbante, T.A. Babrowski, G. Pitoulias, Y. Tshomba, C. Gandarias, A. Badawy, J.-P.P.M. de Vries, Endovascular aortic repair with EndoAnchors demonstrate good mid-term outcomes in physician-initiated multicenter analysis—The PERU registry, Vascular 30 (2022) 27–37, http://dx.doi.org/10.1177/1708538121992596.

[52] H.A. Potter, L. Ding, S.M. Han, F.A. Weaver, A.W. Beck, M.B. Malas, G.A. Magee, Impact of high-risk features and timing of repair for acute type b aortic dissections, J. Vasc. Surg. 76 (2022) 364–371.e3, http://dx.doi.org/10.1016/j.jvs.2022.03.030.

[53] Z. Kostun, M. Mehta, TEVAR and reintervention: How to manage endoleaks and false lumen perfusion, Endovasc. Today 16 (2017) 60–62.

[54] R. Giudice, O. Borghese, G. Sbenaglia, C. Coscarella, C. De Gregorio, M. Leopardi, G. Pogany, The use of EndoAnchors in endovascular repair of abdominal aortic aneurysms with challenging proximal neck: Single-centre experience, JRSM Cardiovasc. Dis. 8 (2019) 2048004019845508, http://dx.doi.org/10.1177/2048004019845508.

[55] R. Romarowski, M. Conti, S. Morganti, V. Grassi, M.M. Marrocco-Trischitta, S. Trimarchi, F. Auricchio, Computational simulation of TEVAR in the ascending aorta for optimal endograft selection: A patient-specific case study, Comput. Biol. Med. 103 (2018) 140–147, http://dx.doi.org/10.1016/j.compbiomed.2018.10.014, URL: https://www.sciencedirect.com/science/article/pii/S0010482518303135.

[56] A. Rinaudo, G.M. Raffa, F. Scardulla, M. Pilato, C. Scardulla, S. Pasta, Biomechanical implications of excessive endograft protrusion into the aortic arch after thoracic endovascular repair, Comput. Biol. Med. 66 (2015) 235–241, http://dx.doi.org/10.1016/j.compbiomed.2015.09.011, URL: https://www.sciencedirect.com/science/article/pii/S0010482515003212.

[57] H.E. Altnji, B. Bou-Saïd, H. Walter-Le Berre, Numerical simulation for design evaluation of thoracic stent graft to investigate the migration phenomena and type 1a endoleak of thoracic aneurysm, J. Vasc. Med. Surg. 3 (2015) 187, http://dx.doi.org/10.4172/2329-6925.1000187.

[58] X. Kan, T. Ma, J. Lin, L. Wang, Z. Dong, X.Y. Xu, Patient-specific simulation of stent-graft deployment in type b aortic dissection: model development and validation, Biomech. Model. Mechanobiol. 20 (6) (2021) 2247–2258, http://dx.doi.org/10.1007/s10237-021-01504-x.

[59] R.M. Romarowski, E. Faggiano, M. Conti, A. Reali, S. Morganti, F. Auricchio, A novel computational framework to predict patient-specific hemodynamics after TEVAR: Integration of structural and fluid-dynamics analysis by image elaboration, Comput. & Fluids 179 (2019) 806–819, http://dx.doi.org/10.1016/j.compfluid.2018.06.002, URL: https://www.sciencedirect.com/science/article/pii/S0045793018302962.

[60] A. Ramella, F. Migliavacca, J.F. Rodriguez Matas, T.J. Mandigers, M. Domanin, D. Bissacco, R.H. Heijmen, S. Trimarchi, G. Luraghi, On the validation of patient-specific numerical simulations of the TEVAR procedure, Procedia Struct. Integr. 49 (2023) 16–22, http://dx.doi.org/10.1016/j.prostr.2023.10.004, URL: https://www.sciencedirect.com/science/article/pii/S2452321623005838. 2nd International Conference on Medical Devices: Materials, Mechanics and Manufacturing (ICMD3M 2023).

[61] A. Ramella, F. Migliavacca, J.F. Rodriguez Matas, T.J. Mandigers, D. Bissacco, M. Domanin, S. Trimarchi, G. Luraghi, Applicability assessment for in-silico patient-specific TEVAR procedures, J. Biomech. 146 (2023) 111423, http://dx.doi.org/10.1016/j.jbiomech.2022.111423, URL: https://www.sciencedirect.com/science/article/pii/S002192902200464X.

[62] Livermore Software Technology, LS-DYNA Keyword User's Manual, Ansys, Inc., Livermore, CA, United States, 2021, URL: https://lsdyna.ansys.com/manuals/.

[63] Blender Online Community, Blender - a 3D Modelling and Rendering Package, Blender Foundation, Stichting Blender Foundation, Amsterdam, 2018, URL: http://www.blender.org.

[64] C. Geuzaine, J.-F. Remacle, Gmsh: a three-dimensional finite element mesh generator with built-in pre-and post-processing facilities, Internat. J. Numer. Methods Engrg. (2009) 1–24, http://dx.doi.org/10.1002/nme.2579.

[65] M.L. Raghavan, D.A. Vorp, Toward a biomechanical tool to evaluate rupture potential of abdominal aortic aneurysm: identification of a finite strain constitutive model and evaluation of its applicability, J. Biomech. 33 (2000) 475–482, http://dx.doi.org/10.1016/s0021-9290(99)00201-8.

[66] E. Abbott, S. Dhara, K. Khabaz, S. Sankary, K. Cao, N. Nguyen, T. Babrowski, L. Pocivavsek, R. Milner, Computational analysis of endovascular aortic repair proximal seal zone preservation with endoanchors: A case study in cylindrical neck anatomy, JVS Vasc. Sci. 2 (2021) 170–178, http://dx.doi.org/10.1016/j.jvssci.2021.06.001.

[67] M. Amabili, K. Karazis, R. Mongrain, M.P. Paï doussis, R. Cartier, A three-layer model for buckling of a human aortic segment under specific flow-pressure conditions, Int. J. Numer. Methods Biomed. Eng. 28 (5) (2012) 495–512, http://dx.doi.org/10.1002/cnm.1484, arXiv:https://onlinelibrary.wiley.com/doi/pdf/10.1002/cnm.1484.

[68] Johnson Matthey, Nitinol technical properties, 2023, https://matthey.com/products-and-markets/other-markets/medical-components/resource-library/nitinol-technical-properties. (Accessed 11 December 2023).

[69] C. Jørgensen, W. Paaske, Physical and mechanical properties of ePTFE stretch vascular grafts determined by time-resolved scanning acoustic microscopy, Eur. J. Vasc. Endovasc. Surg. 15 (5) (1998) 416–422, http://dx.doi.org/10.1016/S1078-5884(98)80203-7.

[70] L. Antiga, M. Piccinelli, L. Botti, B. Ene-Iordache, A. Remuzzi, D.A. Steinman, An image-based modeling framework for patient-specific computational hemodynamics, Med. Biol. Eng. Comput. 46 (2008) 1097–1112, http://dx.doi.org/10.1007/s11517-008-0420-1.

[71] L. Pocivavsek, R. Dellsy, A. Kern, S. Johnson, B. Lin, K.Y.C. Lee, E. Cerda, Stress and fold localization in thin elastic membranes, Science 320 (5878) (2008) 912–916, http://dx.doi.org/10.1126/science.1154069, arXiv:https://www.science.org/doi/pdf/10.1126/science.1154069.

[72] L. Pocivavsek, J. Pugar, R. O'Dea, S.-H. Ye, W. Wagner, E. Tzeng, S. Velankar, E. Cerda, Topography-driven surface renewal, Nat. Phys. 14 (2018) 948–953, http://dx.doi.org/10.1038/s41567-018-0193-x.

[73] T. Ueda, D. Fleischmann, M.D. Dake, G.D. Rubin, D.Y. Sze, Incomplete endograft apposition to the aortic arch: Bird-beak configuration increases risk of endoleak formation after thoracic endovascular aortic repair, Radiology 255 (2) (2010) 645–652, http://dx.doi.org/10.1148/radiol.10091468, arXiv:https://doi.org/10.1148/radiol.10091468. PMID: 20413775.

[74] H.-L. Hsu, C.-K. Chen, P.-L. Chen, I.-M. Chen, C.-P. Hsu, C.-W. Chen, C.-C. Shih, The impact of bird-beak configuration on aortic remodeling of distal arch pathology after thoracic endovascular aortic repair with the zenith pro-form TX2 thoracic endograft, J. Vasc. Surg. 59 (1) (2014) 80–88, http://dx.doi.org/10.1016/j.jvs.2013.07.098, URL: https://www.sciencedirect.com/science/article/pii/S0741521413014109.

[75] M. Boufi, C. Guivier-Curien, V. Deplano, O. Boiron, A. Loundou, B. Dona, O. Hartung, Y. Alimi, Risk factor analysis of bird beak occurrence after thoracic endovascular aortic repair, Eur. J. Vasc. Endovasc. Surg. 50 (1) (2015) 37–43, http://dx.doi.org/10.1016/j.ejvs.2015.04.018, URL: https://www.sciencedirect.com/science/article/pii/S1078588415002609.

[76] J.A. Kratzberg, J. Golzarian, M.L. Raghavan, Role of graft oversizing in the fixation strength of barbed endovascular grafts, J. Vasc. Surg. 49 (6) (2009) 1543–1553, http://dx.doi.org/10.1016/j.jvs.2009.01.069, URL: https://www.sciencedirect.com/science/article/pii/S0741521409002250.

[77] K. Lin, M.L. Raghavan, Study of folding in endovascular grafts due to oversizing, in: ASME 2010 Summer Bioengineering Conference, Parts A and B, 2010, pp. 123–124, http://dx.doi.org/10.1115/SBC2010-19413.

[78] S.B. Ongstad, D.F. Miller, J.M. Panneton, The use of EndoAnchors to rescue complicated TEVAR procedures, J. Cardiovasc. Surg. 57 (2016) 716–729.